Engineering Structures 205 (2020) 110118

Contents lists available at ScienceDirect

Engineering Structures

journal homepage: www.elsevier.com/locate/engstruct

Performance and optimum design of replaceable steel strips in an innovative metallic damper

Wei Guo[a,b,c], Chenzhi Ma[a], Yujie Yu[a,c,*], Dan Bu[d], Chen Zeng[a,b]

[a] School of Civil Engineering, Central South University, Changsha 410075, China
[b] National Engineering Laboratory for High Speed Railway Construction, Changsha 410075, China
[c] Engineering Technology Research Center for Prefabricated Construction Industrialization of Hunan Province, Changsha 410075, China
[d] Hunan Architectural Design Institute Limited Company, Changsha 410012, China

ARTICLE INFO

Keywords:
Passive metallic damper
Experimental test
Seismic performance
Energy dissipation
Finite element analysis

ABSTRACT

In this study, a high efficiency metallic damper with replaceable steel strips and the adjustable construction is proposed for framed structures. The proposed damper uses bolted steel strips as the energy dissipation fuses, which can be adjusted or replaced after failure without affecting the connecting part. The steel strips participate in the load bearing and energy dissipation through an in-plane bending mechanism. In addition, to exert the load bearing and achieve the potential plasticity fully, the steel strips are desired to yield simultaneously and dissipate energy throughout the entire section. In this paper, the primary configuration design method was provided through a theoretical derivation. Further, the nonlinear performance of the proposed fuse strips was evaluated through a series of quasi-static cyclic tests. The influence of the configuration dimensions was investigated through the experimental study and corresponding finite element analyses. The results indicate that the strips successfully exert their potential energy dissipation with pump hysteresis loops. The fuse strips can better participate in the energy dissipation through bending-dominated working mode, and the bending moment strength of the steel strip is mainly controlled based on the width of the central region. The configuration of the transition region greatly affects the failure mode, the plasticity distribution, and the deformation capability. Based on the test data and the numerical simulation investigations, some primary design guidance for the fuse steel strips is suggested.

1. Introduction

In a conventional aseismic design, the building structures need to satisfy a series of requirements regarding the stiffness, strength, and ductility to ensure sufficient resistance and avoid a collapse during an earthquake. Post-earthquake retrofits often reveal that, even though the collapse prevention or the life safety design objectives are satisfied, significant economic losses still occur owing to the severe damage in non-structural elements and minor damage in the structural elements [1–3]. Because seismic energy is mainly dissipated through the plasticity development at the structural members, the damaged buildings are difficult to repair or reuse. A damage control design is thus proposed that aims to transfer the main source for energy dissipation from the structural members to specially designed devices that can be repaired or replaced [4]. Approaches for damage control are mainly classified into three types: active, semi-active, and passive control. Passive energy dissipation designs do not need external power; hence, they are the most economical [5]. Passive energy dissipation designs generally use specially designed dampers that are installed in a structure, normally at places that have large inter-story drift. Under earthquake excitations, the dampers will be activated and dissipate energy through plastic deformation, protecting the structural members from damage at the same time. After an earthquake, the dampers can be replaced easily without modifying the parent structures, thus minimizing the economic loss and interruption to human activities.

There are several types of passive energy dissipation devices such as metallic yielding dampers, friction dampers, and viscous and viscoelastic dampers. In addition, metallic dampers have received considerable attention, and are widely used owing to their simple mechanism and reliable energy dissipating performance. Metallic dampers were first manufactured 50 years ago [6], and since then various metallic dampers have been designed and proposed based on different plastic deformation mechanisms such as tension, bending, shear, torsion, or their combination for energy dissipation. Some well-known metallic

---

[*] Corresponding author at: School of Civil Engineering, Central South University, Changsha, Hunan, China.
E-mail address: yujiecsu@csu.edu.cn (Y. Yu).

https://doi.org/10.1016/j.engstruct.2019.110118
Received 27 February 2019; Received in revised form 2 December 2019; Accepted 18 December 2019

dampers include the added damping and stiffness (ADAS) [7–9] and triangular ADAS (TADAS) [10–12] that participate in energy absorption through the in-plane or out-of-plane bending of steel plates; buckling restrained braces (BRBs) [13–15] that utilize the tensile-compressive yielding of steel cores for energy dissipation; and steel slit dampers (SSDs) [16–19] that provide plastic deformation through planar deformation and a shear-bending mechanism in slit sheets.

Metallic dampers have proven to be an effective tool for damage control and enhancing the energy dissipation of structures. However, the construction of many metallic dampers, particularly for BRBs or steel slit dampers, still incurs certain durability and efficiency problems. Traditional SSDs are generally used in straight steel slits, and these steel strips often have strain concentrations at the roots where low cyclic fatigue failures are often initiated [16,19]. To solve this problem, Ghabraie et al. [20] used a bi-directional evolutionary structural optimization method to develop the optimum configuration of steel slits in an SSD, and found that a middle section with a narrowed shape can increase the working efficiency and eliminate the concentration of stress. Lee et al. [21] compared the cyclic performance of dumbbell-, tapered-, and hourglass-shaped steel strip dampers. In addition, the results indicate that a dumbbell and tapered-shape design can improve the cyclic loading performance and fatigue life of the dampers. Other points recently put forward are the reuse efficiency and the replaceability problem. In many metallic dampers, the effective working region for energy dissipation only accounts for a relatively small portion, similar to the steel core in BRBs. The remaining components in the dampers are often used for the erection and connection to structural members, or for restraining the steel strips from bending or buckling [22]. During an earthquake, only a small portion of the damper will produce a large plasticity, and the majority of the connecting parts or envelop regions will stay within an elastic state. However, owing to an integrated or continuous construction, the entire damper will become obsolete and must be replaced even when only slight damage occurs at certain spots. Considering these questions, several replaceable metallic dampers have been proposed. Aghlara and Tahir [23] designed a bar-fuse damper that uses replaceable bars for energy dissipation. The proposed damper has two box-like parts that being connected with round steel bars. The steel bars are energy-absorbing components and can be easily replaced in the case of a failure, and the remaining parts can all be remained and reused. A similar replaceable idea was also described in a study conducted by Lee and Kim [24]' who proposed a box-shaped steel slit damper for a seismic retrofit, which has a bolted steel slit plate between the interior and exterior casings. In this way, the dampers can minimize the economic loss when damage occurs during the energy dissipation of the cores. Only the effective working parts or damaged cores will be replaced, and the remaining elastic connecting components in the damper can be retained and reused in the retrofit of a building.

In this study, a high efficiency metallic damper with replaceable steel strips and an adjustable design is proposed. The primary construction of the proposed damper is shown in Fig. 1. The damper is designed in a box shape and consists of a rigid inner core and an outer casing. The replaceable steel strips are bolted to the inner and outer parts and provide energy dissipation through a bending mechanism. Differing from most steel dampers that need low yield point steels for early yielding and plasticity for energy dissipation, the steel strip fuses used in this damper can be fabricated using normal structural steel, such as carbon or low alloy structural steel. In addition, the early yielding requirements and the desired energy dissipation ability can be realized through an adjustment of the configuration dimensions of the steel strips. Because the fuse strips are bolted to the damper, they can be easily replaced after failure, and the number and location of the strips can be adjusted according to the design requirements. Moreover, the connecting parts can be reused, thus minimizing the cost for the refabrication of the damper. Fig. 2 shows suitable application conditions for the proposed damper. The new damper can be installed in the middle and end parts of the diagonal and chevron braces. Therefore, as an advantage compared to other metallic dampers, the installation of this damper also has fewer limitations.

In the proposed damper, the replaceable steel strips are the source of the energy dissipation. In this study, the primary design and configuration optimization of the fuse strips used in the proposed damper were investigated. The seismic performance, the influencing pattern of the strip configurations on the cyclic behaviors, and the energy dissipation abilities of the steel strips were investigated and evaluated through a series of quasi-static cyclic experiments and numerical simulations. Based on the results obtained, some preliminary suggestions on the design of steel strips and innovative dampers are presented.

2. Design and configuration optimization of the fuse strips

2.1. Optimum section width calculation

Fig. 1 shows that the designed steel strip fuses utilize four-point bending loading mode with two outer ends of the strip being bolted to the outer casing, and the inner two spots being bolted to the inner core. Fig. 3(a) illustrates the detailed configuration of an individual steel strip, and Fig. 3(b) shows a moment diaphragm at a steel strip under a lateral displacement load. Under the relative movement between the inner core and the outer casing, the steel strips will produce a moment condition that linearly increases the moment from support A to B (or from support D to C), as shown in Fig. 3(a), and a constant moment along the BC region, as given in Fig. 3(b).

Previous studies on steel slit dampers indicate that the moment level and the extent of plasticity development along the steel strip are closely related to the geometrical dimensions. With a good configuration and an optimum fuse design, the steel slits can avoid unfavorable stress concentrations, and the entire section can participate in the energy dissipation. To reach a high working efficiency, it is desirable that the steel strips enter yielding and plasticity simultaneously throughout the entire region of the steel strip. Hence, the section configuration of the fuse strips in the new damper also require an appropriate design to exert the load bearing and potential plasticity development fully.

A strip designed with the section width based on the moment diaphragm can facilitate a uniform strain development and simultaneous yielding throughout the entire region. Based on this idea, the relations between different configurations of the dimensions in the optimized design can be obtained through a theoretical derivation. As shown in Fig. 3(b), given distance x from any spot in the strip to the left support A, and P as the reaction force at support A, the moment M_x at location x can be obtained as follows:

$$M_x = Px \tag{1}$$

In addition, when the entire section enters a yielding state, the plastic moment $M_{px}$is as follows:

$$M_{px} = f_y W_{px} = f_y \frac{th_x^2}{4} \tag{2}$$

Here, f_y is the yield strength of steel, W_{px} indicates the entire section plasticity coefficient, t is the thickness of the steel strip, and $h_x$is the section width at spot x. In an optimum strip design, different spots along the strip can enter a yielding state at the same time, which implies a relation of $M_x = M_{px}$, and the optimum configuration width $h_x$can be obtained as follows:

$$h_x = 2\sqrt{\frac{Px}{f_y t}} \tag{3}$$

Eq. (3) indicates that the optimum width of a strip in transition regions AB and CD follows a parabolic pattern under a constant strip thickness. However, the above derivations on the section width calculation are only based on the ideal bending mode. In addition, the section width h_0 reduces to zero at the two ends based on Eq. (3), which is

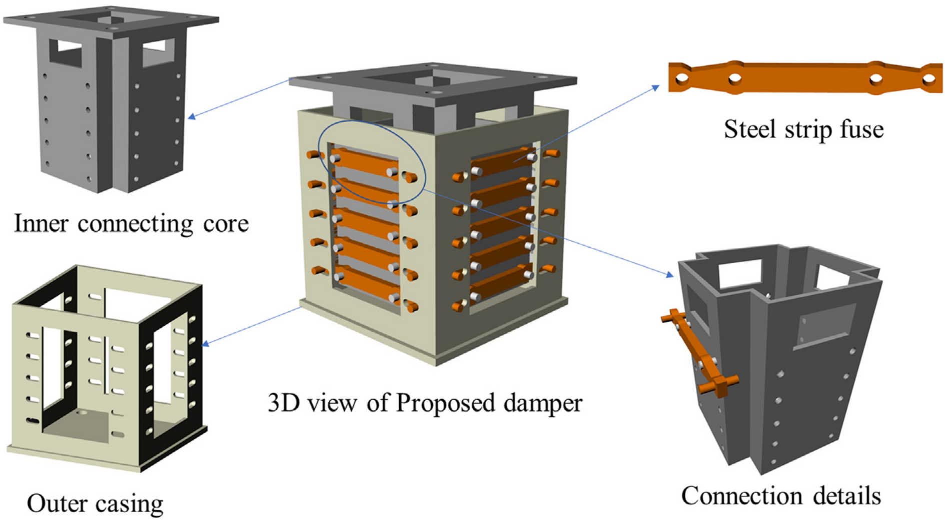

Fig. 1. Schematic diagram of the proposed steel strip damper.

unpractical in a real design. Except for the bending moment, a considerable resultant shear force also occurs in the transition region, and a shear failure is undesired. A minimum section width then exists in the transition region to ensure that no shear failure develops ahead of the full section plasticity. Here, we supposed that the strip ends should be able to resist at least twice the reaction shear at the end section. Then, the minimum section width at end section $h_{\min}$ can be obtained as follows:

$$\frac{f_y h_{\min} t}{\sqrt{3}} = 2P \tag{4}$$

$$h_{\min} = \frac{\sqrt{3} h_1^2}{2b_1} \tag{5}$$

where b_1 represents the distance between supports A and B, and h_1 provides the section width at the center region.

2.2. Theoretical analysis of yield strength and stiffness

Because the fuse strips in the damper participate in the load bearing through a shear-bending mechanism, the bending-dominated, shear-dominated, or a shear-bending working mechanism may occur based on different combinations of configuration dimensions. In addition, the yield strength, the elastic stiffness, and the failure modes are also closely related to the section configurations. For example, in a damper with long steel strips, the working state at the steel strips will be bending-dominated with a relatively large elastic deforming ability and a smaller damper stiffness. In this section, the yield strength of a steel strip is calculated, and the relation between the lateral stiffness and configuration dimensions is discussed.

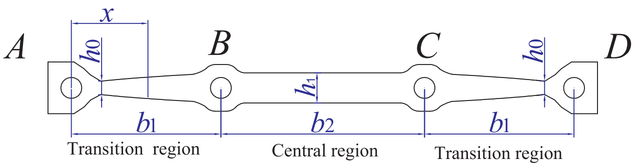

(a) Geometric illustration of the steel strip

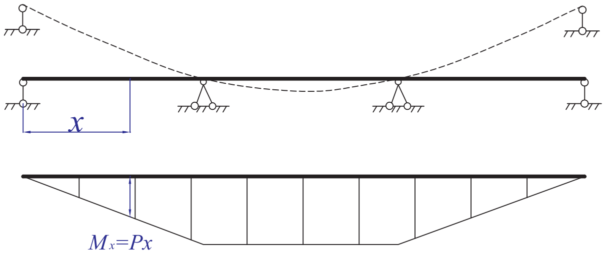

(b) Moment diaphragm along the steel strip

Fig. 3. Configuration design of the steel strip in the proposed damper.

In the bending-dominated case, the required lateral reaction force at the supports was determined through the moment bearing performance

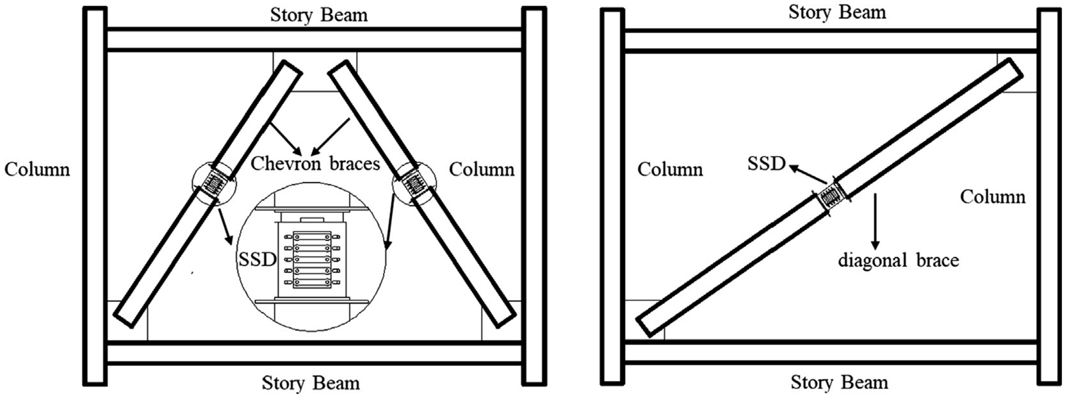

Fig. 2. Possible configurations for installation of steel strip damper in a frame.

along the strip. In addition, the reaction force during the entire section plastic state P_m can be calculated through a transformation of Eq. (3):

$$P_m = \frac{M_{px}}{b_1} = \frac{f_y t h_1^2}{4b_1} \tag{6}$$

However, in the shear-dominated case, the reaction force during yielding state P_s will lead to any section undergoing shear yielding. Given that the tension yield strength of steel is$\sqrt{3}$ times the shear yield strength, and considering the averaged shear stress distribution along the section, the following equation can be obtained:

$$P_s = \frac{f_y}{\sqrt{3}} \cdot \frac{2}{3} t h_1 = \frac{2 f_y t h_1}{3\sqrt{3}} \tag{7}$$

As illustrated early, the fuse strips were designed to participate in the load bearing and energy dissipation through lateral bending, and no shear failure is desired ahead of the bend yielding. Hence P_s needs to be larger than P_m, and a basic relation between section dimensions can be obtained.

$$b_1 > \frac{3\sqrt{3}}{8} h_1 \tag{8}$$

In addition, the yield strength of a damper with n strips F_n can be calculated as follows:

$$F = n \min\{P_m, P_s\} = n \frac{f_y t h_1^2}{4b_1} \tag{9}$$

At the given reaction force, the induced moment along the strip can be obtained, and the resulting displacement δ at the supports can be obtained through the virtual work principle:

$$\delta = \int_0^{\frac{L}{2}} \frac{\overline{M} M_{px}}{E I_x} dx + \int_0^{\frac{L}{2}} \frac{\overline{V} V_x}{G A_x} dx = \frac{12P}{Et} \int_0^{\frac{L}{2}} \frac{x^2}{{h_x}^3} dx + \frac{P}{Gt} \int_0^{\frac{L}{2}} \frac{1}{h_x} dx \tag{10}$$

where E and $G$are the elastic modulus and shear modulus of steel, $I_x$is the section moment inertia, A_x the section area at section x, and L provides the entire length of the strip. The stiffness of an individual strip K_e can be obtained as follows:

$$K_e = \frac{P}{\delta} = \frac{1}{\left\{\frac{12}{Et}\int_0^{\frac{L}{2}} \frac{x^2}{h_x^3} dx + \frac{1}{Gt}\int_0^{\frac{L}{2}} \frac{1}{h_x} dx\right\}} \tag{11}$$

From Fig. 3, a dimensional relation can be indicated as $b_1 + \frac{b_2}{2} = \frac{L}{2}$, and the section width has a different range of expression in b_1 and b_2, as indicated in Eq. (12).

$$\begin{cases} h_x = \frac{h_1 - h_0}{b_1} x & 0 < x < b_1 \\ h_x = h_1 & b_1 \leqslant x \leqslant b_2/2 \end{cases} \tag{12}$$

Given k as the ratio of h_0 to h_1, the stiffness expression in Eq. (11) can be calculated as follows:

$$K_e = \frac{1}{\left\{\frac{6}{Eth_1^3}\left[\frac{(k-3)}{(k-1)^2} + \frac{2\ln(k)}{(k-1)^3} + b_1^2 b_2 + \frac{b_1 b_2^2}{2} + \frac{b_2^3}{12}\right] + \frac{1}{Gth_1}\left[\frac{b_1 \ln(k)}{(k-1)} + \frac{b_2}{2}\right]\right\}} \tag{13}$$

Eq. (13) is a complicated equation, but it can reveal the relation of the lateral bearing stiffness versus the configuration of the dimensions. The stiffness is inversely proportional to the square of b_1 or the cubic of b_2. Moreover, the stiffness is proportional to the cubic of h_1, or to the thickness t.

The design and stiffness of the steel strip had two extreme conditions. In the first case, the length of the transition region b_1 equals zero. There were no intermediate supports B and C, and the steel strip was degenerated into a steel plate with a constant width. Under this case, the steel strip has the maximum lateral stiffness, as in Eq. (14), and the steel strip behaves like a two-ended fixed beam.

$$K_e^{b_1=0} = \frac{2}{\frac{{b_2}^3}{E{h_1}^3 t} + \frac{b_2}{G h_1 t}} \tag{14}$$

Under another extreme condition in which the length of the central region b_2 decreased to zero, the steel strip in Fig. 3 was degenerated into a three-point support case. Under this condition, the steel strip has the maximum deforming ability with the smallest stiffness (Eq. (15)). In addition, the fuse strip behaves like a beam that is fixed at the center and has a cantilever loading form at either half side.

$$K_e^{b_2=0} = \frac{1}{\left\{\frac{6}{Eth_1^3}\left[\frac{(k-3)}{(k-1)^2} + \frac{2\ln(k)}{(k-1)^3}\right] + \frac{1}{Gth_1}\left[\frac{b_1 \ln(k)}{(k-1)}\right]\right\}} \tag{15}$$

However, a more general case is the configuration shown in Fig. 3, in which the stiffness varies between the values calculated from Eqs. (14) and (15).

The above derivations are all based on the elastic assumptions that the failure modes are calculated under a simultaneous yielding state of all sections or under a shear yielding state. However, during a real application, the steel strips are designed to be loaded under a nonlinear state, and participate in the energy dissipation through the development of plasticity. Once yielding occurs, a plastic stress redistribution takes place in which the above derivations and dimensional relations may no longer be applicable. Moreover, the theoretical derivations were conducted based on the ideal configuration without considering the design of supporting regions. However, the steel strip was bolted to the inner and outer boxes under a practical application (Fig. 3), and the two end and intermediate supports all have a ring configuration with an enlarged section to realize a bolted connection. Therefore, the internal force distribution and yielding development in the strip will not exactly follow the theoretical assumptions. However, the configuration relations in Eqs. (5) and (8), and the strength and stiffness relations in Eqs. (9) and (13), can still be used to help with the preliminary design of the steel strips.

3. Experimental investigation

3.1. Test specimens

Because the nonlinear working state, the failure mode, and the practical energy dissipation ability of the steel strip are difficult to obtain through a theoretical derivation, a series of quasi-static cyclic tests were conducted on individual steel strips to reach a further understanding of the proposed damper. A total of 10 steel strip specimens were designed, with the dimensions of the critical section fulfilling the basic requirements in Eqs. (5) and (9), the detailed constructions and dimensions of which are shown in Fig. 4.

The shape of the transition region (region b_1 in Fig. 3), the lengths of b_1 and b_2, and the widths of h_0 and h_1 were all investigation subjects in the study. Detailed information on the configuration of the tested specimens is provided in Table 1. The diameter of the hinge support was 8 mm, and the spared erection holes at the steel strip had a diameter of 8.4 mm. Specimens SS5 and SS6 had an enlarged intermediate connecting region with an outer arc radius of 11 mm (the other specimens had a radius of 9 mm). The theoretical derivation suggests a parabolic edge at the transition region to ensure the development of uniform and simultaneous plasticity. However, the configuration optimizations during the specimen design process revealed that the parabolic curve obtained was similar to a straight transition when the widths h_0 and h_1 were determined. Therefore, two specimens SS1 and SS2 with an identical configuration of their dimensions were designed. The only difference between the two specimens was the shape of the transition, in which SS1 had parabolic edges and SS2 had straight edges in the transition region. Moreover, for further convenience in their engineering applications and specimen fabrication process, the remaining specimens (SS2–SS10) all had straight b_1 transitions. The tested steel

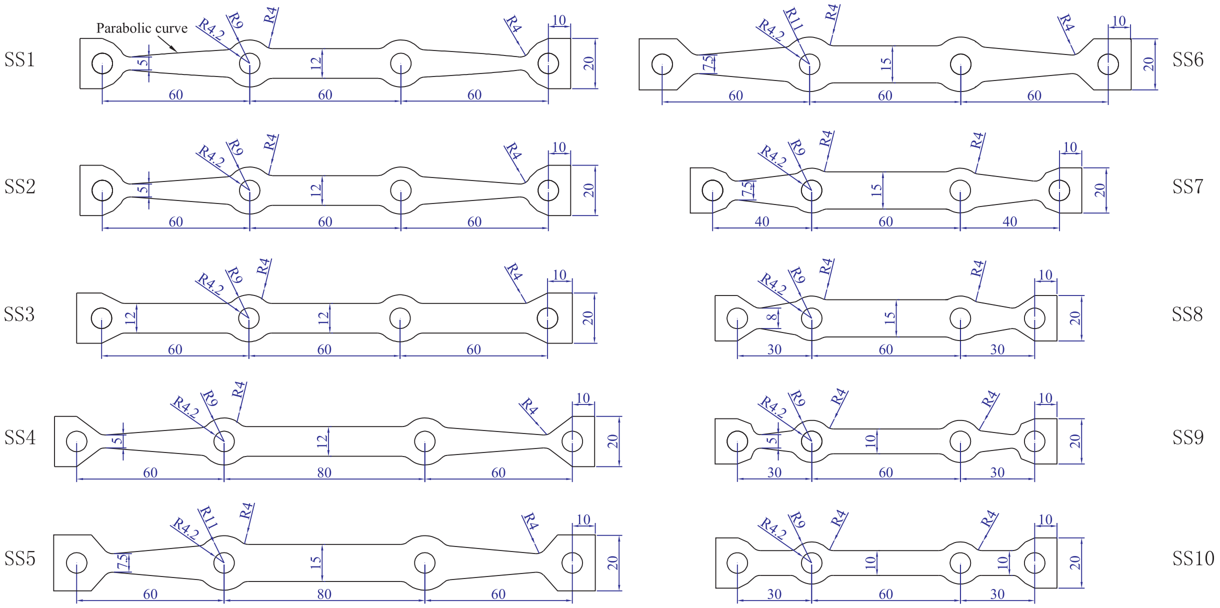

Fig. 4. Configuration of dimensions of tested steel strips.

Table 1
Specimen information (unit in mm).

Specimen No.	b_1	b_2	h_0	h_1	Transition
SS1	60	60	5	12	Parabolic
SS2	60	60	5	12	Straight
SS3	60	60	12	12	Straight
SS4	60	80	5	12	Straight
SS5	60	80	7.5	15	Straight
SS6	60	60	7.5	15	Straight
SS7	40	60	7.5	15	Straight
SS8	30	60	8	15	Straight
SS9	30	60	5	10	Straight
SS10	30	60	10	10	Straight

Table 2
Specimen information (unit in mm).

Grade	Elastic modules E (MPa)	Yield strength f_y (MPa)	Ultimate strength f_u (MPa)	Elongation (%)
Q235	2.04×10^5	402	589	42

strips were all made of Q235 carbon steel, with a nominal design yield strength of 235 MPa. The practical steel strength was tested prior to the damper tests conducted under standard metallic material tensile tests, and the mechanical properties obtained are as listed in Table 2.

3.2. Test setup and loading plan

The quasi-static cyclic tests were performed at a structural lab in Central South University, China. A steel strip was installed between two pairs of hinged loading arms, which can be adjusted according to the length of the specimens (Fig. 5(a)). The inner loading arms were fixed to the reaction frame, and the outer pair was connected to the actuator. The cyclic displacement load was provided with the actuator, which can provide a maximum dynamic load of ± 72 kN.

The cyclic displacement load was applied under a gradually increasing mode with a displacement amplitude of 5 mm, and the loading cycle was repeated once during each loading amplitude (Fig. 5(b)). Using the testing method in Fig. 5(a), the applied displacement will not always be right of the neutral axis of the specimens. When the specimens undergo a large bending deformation, the applied load produces longitudinal component forces along the length direction, the forces of which result in additional tension stress in the strip other than a pure bending reaction. Hence, a maximum bound of (b_2/2–10) mm was settled to the loading protocol. The test was terminated once the maximum displacement was reached or a dramatic strength loss occurred (lateral strength of lower than 85% of the maximum strength) owing to a fracture or buckling failure.

3.3. Test results

Fig. 6 shows the deformation conditions or the failure modes upon the completion of the testing. The tested steel strips all displayed stable and pumped hysteretic loops with a gradual transition from an elasticity to a plasticity developing regime. For specimens SS1, SS2, and SS4, the steel strips presented a bending deformation along the entire length. As shown in Fig. 6(a), the tested specimen SS1 was compared with the untested specimen SS2, and the comparison revealed that the bending deformation was not only present in the central b_2 region, considerable plastic deformation also occurred in the transition b_1 region. This deforming pattern fulfills the desired load-bearing mode in which the entire region of the steel strip can participate in the plasticity development and energy dissipation. SS4 has a longer b_2 region than that of SS1 and SS2, and the central b_2 part displayed a larger range of plasticity development with an obvious metallic luster and distributed ductile cracks at the margin. Specimens SS3 and SS10 demonstrate a uniform width at both the central and transition regions. Under lateral loading, the central part was the main source of the plasticity development. Specimen SS3 had a relatively shorter b_2 region, resulting in a higher plastic bending deformation at the central region under the same lateral displacement. The distributed ductile cracks initiated under the high level of tensile or compressive strain at the section margin. The fatigue failure eventually occurred under the cyclic loading where the initial defects located. A similar low cycle fatigue failure under the high level of cyclic plasticity was also displayed in specimen SS6, although the fracture was close to the intermediate connecting ring.

Most of the specimens had the same configuration design at the connecting rings, with a radius of the inner and outer arches of 4.2 and 9 mm, respectively. This ring width design demonstrated a satisfactory connection for the majority of the tests, except for specimens SS7 and SS8, in which a fracture occurred at the ring part. The reasons for this failure can be seen from the dimensional configuration shown in Fig. 4

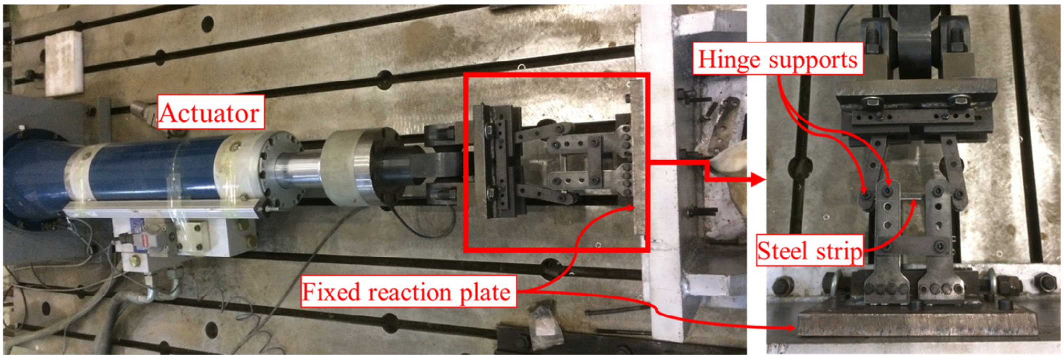

(a) Test setup

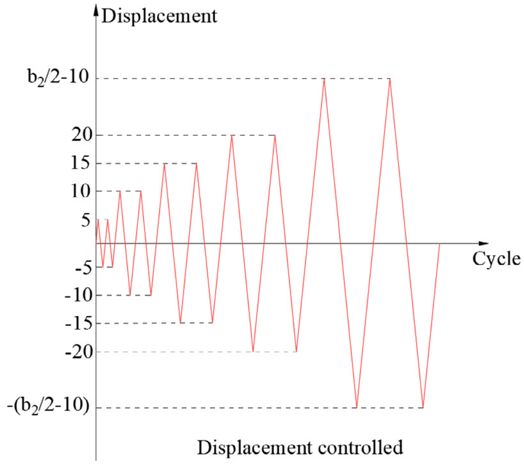

(b) Loading protocol

Fig. 5. Test setup and loading plan.

(a) SS1 (b) SS3 (c) SS4

(d) SS6 (e) SS7 (f) SS9 (g) SS10

Fig. 6. Deformation and failure conditions.

and the obtained hysteretic loops demonstrated in Fig. 7. Specimens SS7 and SS8 showed a wide central region (h_1 = 15 mm) and a relatively short transition region (b_1 = 40 mm and 30 mm). The reaction force and induced moment under the same lateral displacement were therefore higher than those of the other specimens (Fig. 7(c)). The resulting large reaction force led to an extrusion deformation at the connecting ring (Fig. 6(e)). Fig. 8 shows a schematic plot of the resulting internal force at the connecting ring. Owing to the ring construction, a high lateral reaction force will lead to a high tension-compression force at the ring parts. Together with the large extrusion stress from the supports, a complex combination of stresses will be formulated, eventually leading to a fracture failure at the connecting ring in specimens SS7 and SS8. Specimen SS9 had the same h_0 design as specimens SS1 and SS2, but a shorter length of b_1, leading to a larger rotation demand, higher reaction forces, and a faster moment increase along the transition region under the same lateral displacement. Therefore, an excessive plastic bending deformation was developed, and specimen SS9 failed owing to a ductile fracture in the transition region.

3.4. Test data analysis

During the test, the applied load, recorded using a sensor inside the actuator, was twice the reaction force at the outer support. Fig. 7 shows the obtained hysteretic relations of the lateral reaction force versus the applied displacement. Specimens SS1 and SS2 showed nearly the same lateral strength (Fig. 7(a)), indicating that a steel strip with a straight transition can produce a similar lateral strength development and energy dissipation as a parabolic transition. Therefore, in a further application, the parabolic transition region can be simplified and replaced with a straight edge design.

Specimens SS1–SS4 had different combinations of the configuration, but the similar lateral strength developments were presented. Together with the deformation condition and failure modes shown in Fig. 6(a)–(c), for the steel strip design of SS2, the 5 mm design for h_0

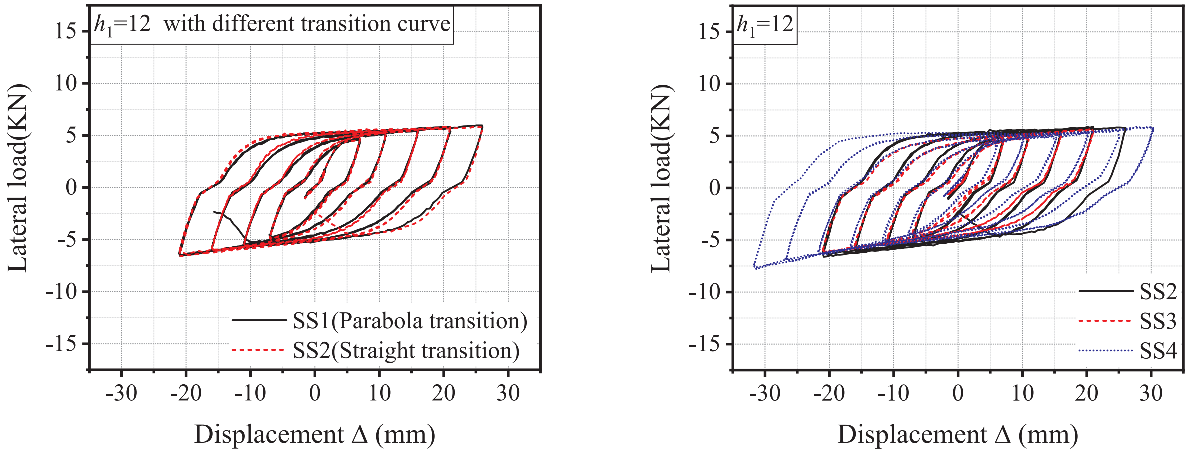

(a) Effect of transition region configuration

(b) Specimens with a h_1 width of 12 mm

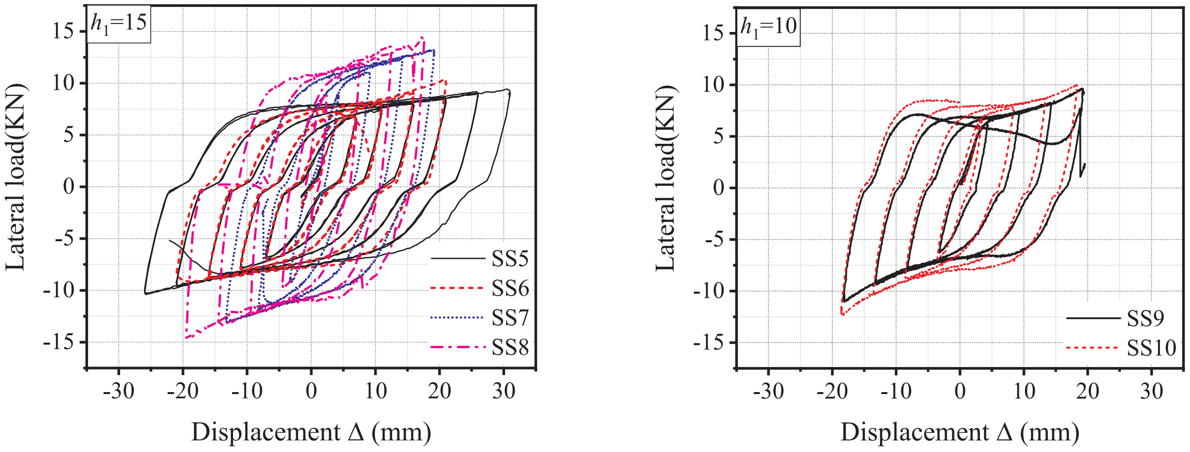

(c) Specimens with a h_1 width of 15 mm

(d) Specimens with a h_1 width of 10 mm

Fig. 7. Hysteretic relations of lateral reaction force versus displacement.

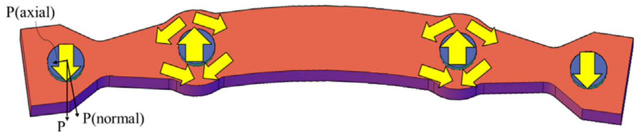

Fig. 8. Internal force flow resulting at inner connecting ring.

can already provide sufficient shear resistance at the edge supports. A further enlarged h_0 (specimen SS3) presented a limited strengthening effect under the lateral strength development, and the bending moment strength of the steel strip was mainly controlled through the width of the central region. The comparison also indicates that the length increases in the central region (b_2) presented a limited influence on the lateral resistance. Nearly the same reaction force was shown between SS2 and SS4 (h_1 = 12 mm, in Fig. 7(b)), and between SS5 and SS6 (h_1 = 15 mm, in Fig. 7(c)).

To better present the moment condition of the specimens, the induced moment at the central region was calculated (by multiplying the reaction force with b_1) and compared, as indicated in Fig. 9. In Fig. 7(c), the short b_1 specimen (SS7) had higher reaction force levels, whereas the resultant moment developments in the central region of SS5–SS7 were similar with each other (Fig. 9(a)). The specimens compared in Fig. 9(b) all showed a bending-dominated deformation pattern, and the moment strengths obtained were increased as the width h_1 in the central region increased. A comparison of the lateral reaction forces and the resultant moment in specimens SS5–SS7 indicated that the loading bearing ability of the steel strips is controlled by the section width and the moment strength in the central part. The transition length b_1 can be used to transform the moment bearing ability of individual strips to the yielding and strength development of the entire damper. Under the same h_1 construction, an increase in the length of b_1 can reduce the resultant reaction forces in individual strips and thus realize a low yield strength of the damper. Specimen SS8 possess an even shorter transition region (b_1 = 30 mm) than that of SS7, leading to a higher reaction force and extrusion deformation at the connecting ring. Under the same lateral displacement between the inner and outer rings, the local plastic deformation at the ring ribs share part of the applied lateral displacement, thus reducing the plastic deformation in the strip. Eventually, a smaller moment strength was developed in SS8, as indicated in Fig. 9(a).

3.5. Energy dissipation efficiency

The tests involved specimens with different configurations, and the most important index for the dampers is the energy dissipation ability and efficiency. To achieve an efficient and comprehensive comparison of the energy dissipation ability, two coefficients were obtained and calculated from the hysteretic relations. One coefficient is the equivalent viscous damping coefficient h_e, which is generally used to evaluate the energy dissipation ability at different drift ratios or load levels. The definition of h_e is given in Fig. 10. The loop delineated by point ABCD is

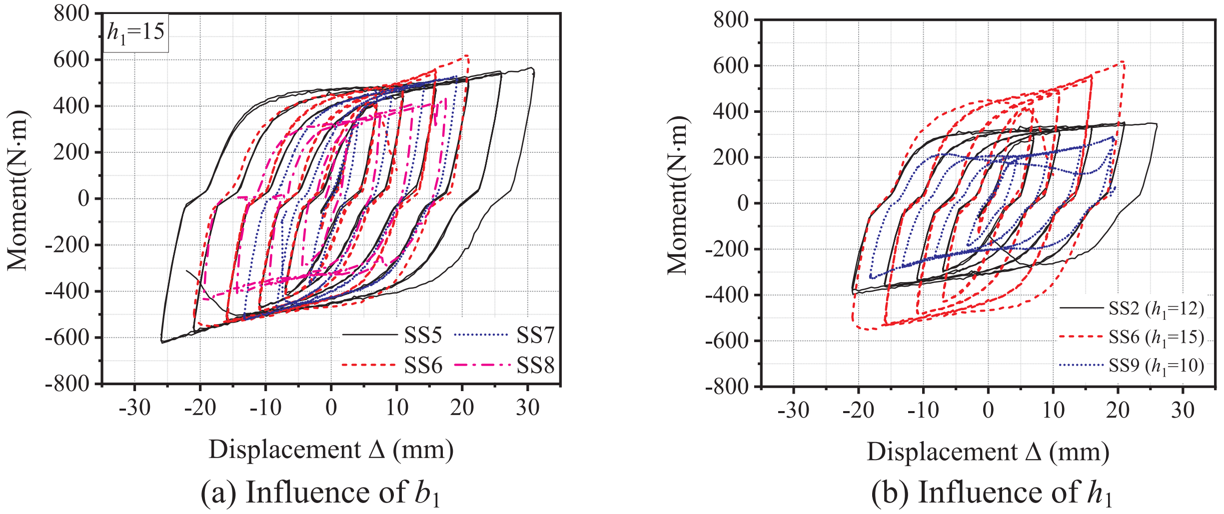

(a) Influence of b_1

(b) Influence of h_1

Fig. 9. Hysteretic relations of induced moment versus displacement.

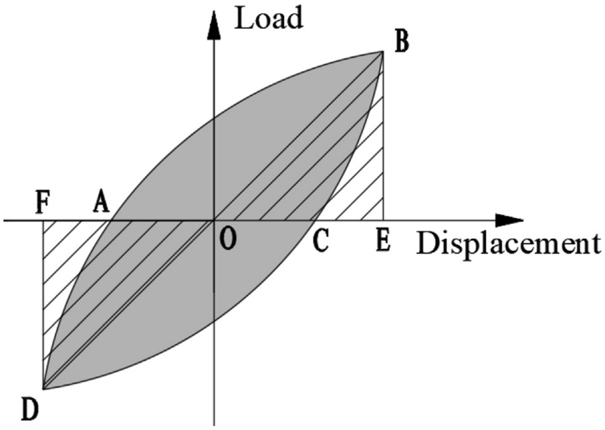

Fig. 10. Definition of the equivalent viscous damping coefficient $h_{e.}$

a complete cycle of the hysteretic curve, and the enclosed area represents the dissipate energy E_d during the loading cycle. The equivalent viscous damping coefficient is defined as follows:

$$h_e = E_d/2\pi S_{(\triangle OBE+\triangle ODF)} \tag{16}$$

where $S_{(\triangle OBE+\triangle ODF)}$ is the sum of the triangle areas OBE and ODF, which represents the reference elastic strain energy corresponding to the identical peak strengths. By contrast, the steel strips are desired to present a high efficiency allowing the entire section of the steel strip to participate in the energy dissipation. Therefore, another coefficient was compared, called the energy density, η, and was defined as the ratio of E_d to the section area S of the strip. In this study, section S was calculated using the section dimensions in Table 1 and the following equation, which simplifies the contributions at the connecting rings.

$$S = (h_0 + h_1)b_1 + h_1 b_2 \tag{17}$$

Fig. 11 shows the two energy coefficients of the second cycle at lateral displacements of ± 15 and ± 20 mm. To make the Fig. 11 be more comprehensible, parameter of a specimen is attached after the specimen number. For example, 1-60/60-5/12-P means the specimen number is SS1 and the parameters of b_1, b_2, h_0, h_1 and transition type are 60 mm, 60 mm, 5 mm, 12 mm and Parabolic, respectively. Specimens SS7 and SS8 showed an early fracture failure at the connecting ring before the completion of ± 20 mm cycles, hence there were no energy coefficients for specimens SS7 and SS8 at ± 20 mm displacement level. Specimens SS9 and SS10 showed a thinner central region, but the energy density η was higher than in the others. However, the equivalent viscous damping coefficient decreased with an increase in the lateral displacements. SS8 possessed high equivalent damping coefficients and energy densities while the two indexes of SS7 stayed at the medium levels. The different results indicate the unstable load bearing and energy dissipation abilities due to the fracture failure occurring at the ring ribs in SS7 and SS8. Specimens SS3 and SS4 presented a lower energy density than the other specimens, and relatively unstable variations in the equivalent viscous damping coefficient. Among the 10 specimens, SS1-2 and SS5-6 all presented a better performance for the damper application owing to the stable increase in the two energy coefficients as the lateral displacement increased.

4. Finite element analyses

4.1. Finite element models

To further understand the internal stress distribution and plasticity development along the steel strips, corresponding finite element models were established using ABAQUS/Standard software. The finite element model included a steel strip and central bolt-supports to consider the contact extrusion effect on the intermediate connecting rings. Owing to the symmetricity, only one half of each steel strip was established, and a symmetrical slidable boundary was settled for the central surface (Fig. 12). The geometrical dimensions and loading pattern of the finite element model were all in accordance with those utilized during the test.

A three-dimensional eight-node solid element C3D8R was used for both the steel strip and the support rod. The element uses reduced integration modes and an hourglass control to avoid the spurious solutions that result from the shear locking and hourglass shape. Surface-to-surface contacts with a normal property of “hard contact” and a “penalty” tangential behavior (with a friction coefficient of 0.1) were applied to the interaction surfaces between the inner surface of the intermediate connecting ring and the support rod. Because no obvious deformation or damage occurred at the outer connecting rings during the tests, the outer support was simplified as an ideal hinge. In the FEM modelling, the inner surface of the ring was coupled to a reference point located at the center of the circle (Fig. 12(a)). Under this coupling constraint, the inner surface of the connecting ring will rotate around the center reference point as a rigid surface. The reference point was only restrained at the out-of-plane displacement freedoms and at the out-of-plane bending rotation, allowing the free in-plane rotation and displacement to realize a moveable hinged outer support boundary. The intermediate rod had a fixed boundary, and a cyclic vertical displacement load was applied at the coupled central point.

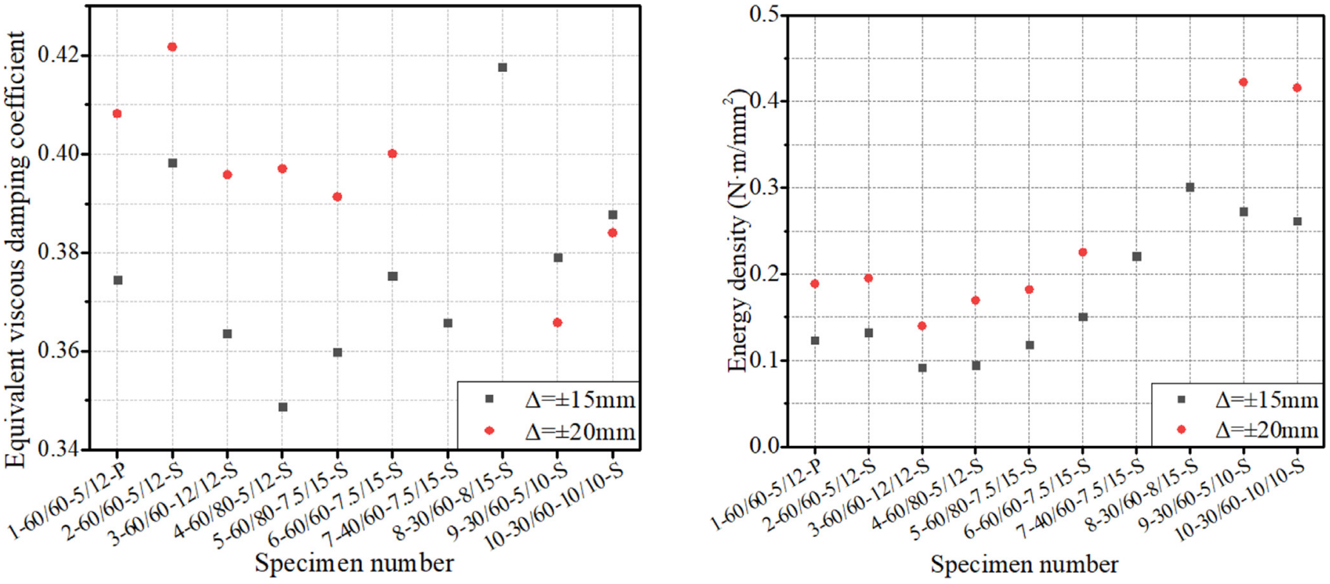

(a) Equivalent viscous damping coefficient (b) Energy density

Fig. 11. Evaluation of energy dissipation ability.

The measured material strengths in Table 2 were adopted during the simulation. The Poisson ratio of the steel material was determined to be 0.3. In addition, to predict the steel plastic strength development under cyclic loading more effectively, a combined hardening material model with four back-stress coefficient pairs was applied for the steel strips. This material model was based on the Chaboche theory and can describe the kinematic and isotropic cyclic hardening behaviors of steel materials. Because no cyclic coupon tests were conducted during the study, the elastic modulus and yield stresses were determined based on the tensile test data, and the hardening parameters were determined based on the Q235 steel data from a previous reference [25]. Von-Mises stress criteria were adopted for all materials, and the Newton–Raphson method was chosen for the solver.

4.2. Comparisons of the results and discussion on design optimization

Figs. 13 and 14 show the hysteretic lateral load versus displacement relations and the Von Mises stress conditions from finite element simulations. Specimens SS1–SS6 were all bending-dominated, and the finite element models can basically reflect the lateral resistance and plasticity development. With a gradually reduced section in the transition region, the entire range of the steel strip participated in the energy dissipation with a better deforming ability. For instance, specimen SS3 showed a uniform width in the transition region, and a high-level plasticity mainly concentrated in the central region (specimen SS3 in Fig. 14). The repeated cycles at such a high plastic strain eventually facilitated an early fracture in SS3 (Fig. 6(b)).

From Fig. 14, it can be found that the stress state of SS6 at the transition strip, and the stress state of SS7 at toe between the ring support and the central strip are more severe than other locations, which distribution is different with the failure locations in the test (Fig. 6(d) and (e)). This inconsistency between the test data and the numerical results of SS6 and SS7 may be attributed to the limitation of FEM and the possible manufactory defect at the ring toe. It should be noted that the fracture properties of the material are not established in present finite element models, which means the FEM cannot predict the crack, fracture failure and the initial notches in the material. The specimens were designed to have smooth transition, but initial notches may exist from the fabrication process. Once the stress level around the ring rib reaching or being close to the ultimate strength, fatigue failure is likely to occur under the high level of cyclic plasticity or the high stress state. But this defect is not considered and the induced failure cannot be simulated in present FEM. However, the finite element models are still effective that they can basically reflect the lateral resistance and plasticity development, from which the stress-state and effective working mechanism can be indicated. Moreover, the high stress regions in FEM results also correspond to weak locations in the steel strip where failure occurred.

Among all simulations conducted, specimens SS8–SS10 presented an excessive hardening effect compared with the test data. This difference might be attributable to the excessive plastic deformation and the boundary settings. Specimens SS8–SS10 had a short transition region (30 mm), and the bending rotation in the transition region was larger than that of the other specimens under the same lateral displacement. The higher rotational demand led to the development of an excessive plastic deformation. The high level of plasticity was concentrated at the connecting ring in SS8, in the transition region in SS9, and at the central region in SS10. The high level of developed plasticity

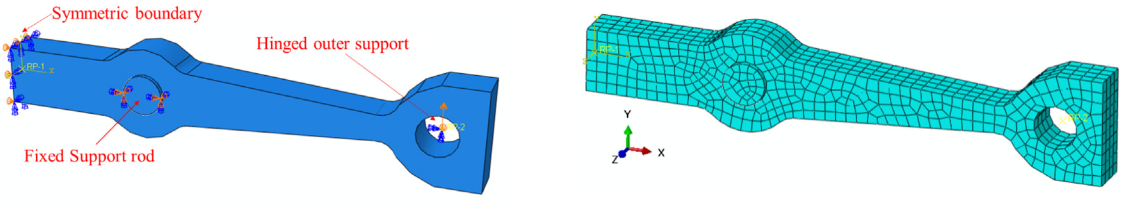

(a) Finite element model (b) Meshed model

Fig. 12. Established finite element model in ABAQUS (SS2).

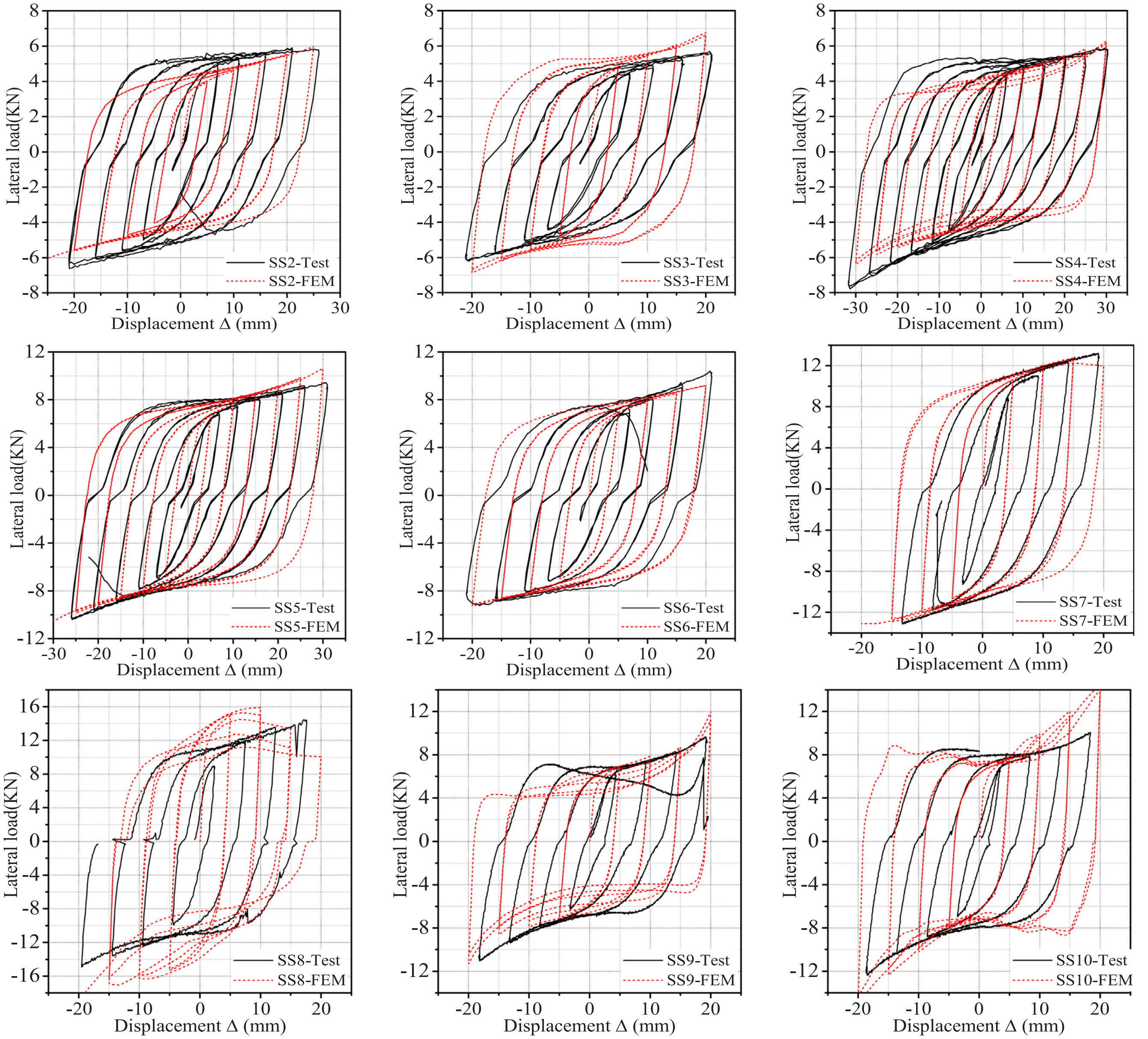

Fig. 13. Hysteretic curve comparing finite element results to the test data.

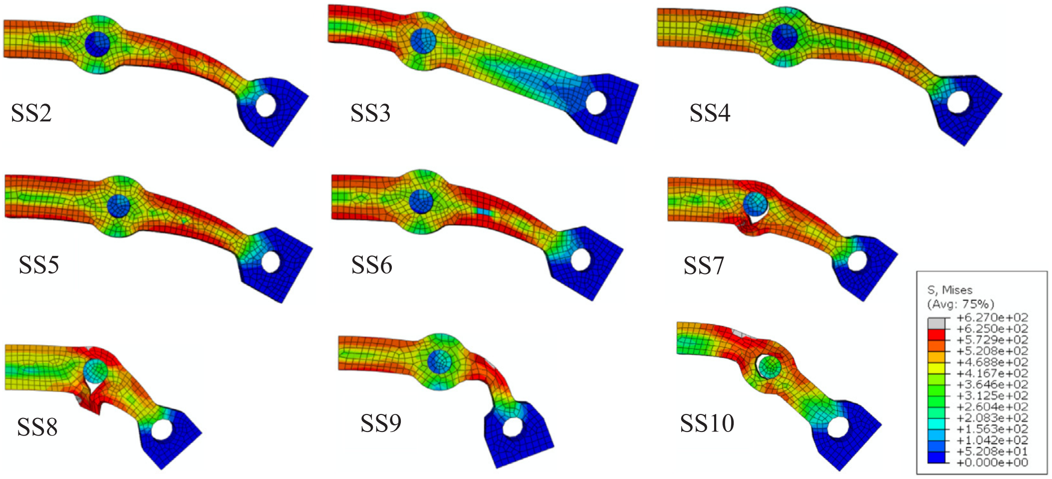

Fig. 14. Von Mises stress distribution and deformation condition (Δ = 20 mm).

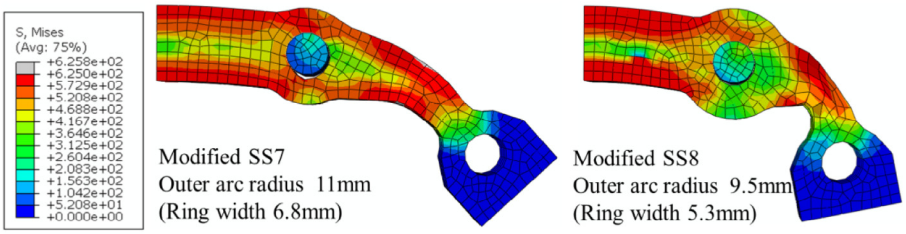

(a) Von Mises stress distribution of modified SS7 and SS8 (Δ = 20 mm)

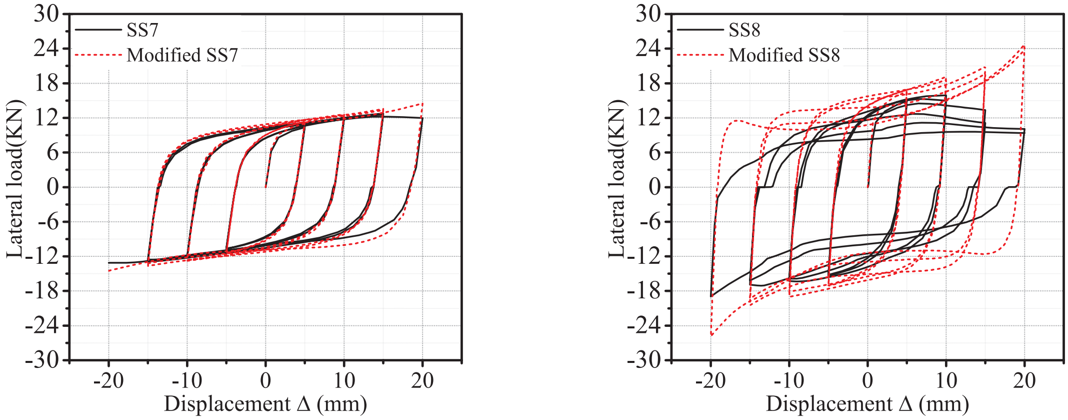

(b) Comparison of hysteretic relation

Fig. 15. Performance of modified SS7 and SS8 (Δ = 20 mm).

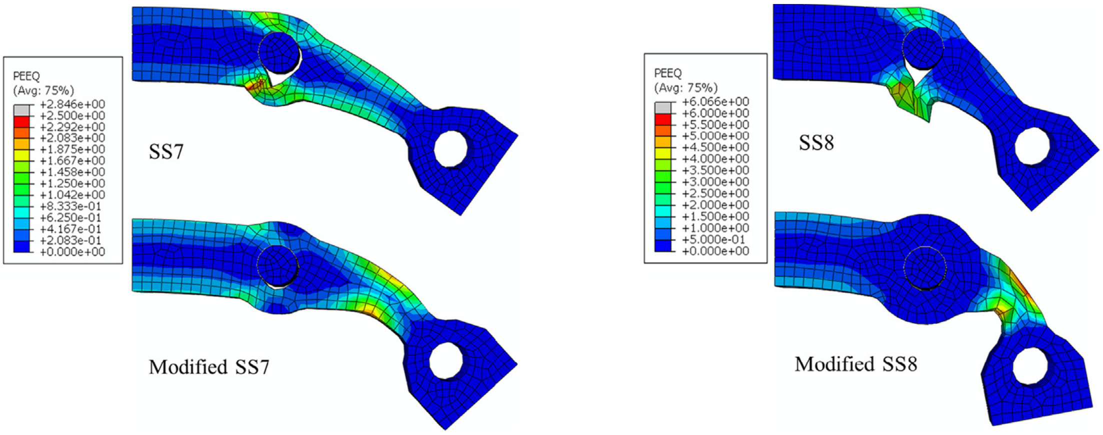

Fig. 16. PEEQ index conditions (Δ = 20 mm).

caused an elongation effect on the specimens. While in the FE models, the three-directional displacements of the inner support rod were fixed to ensure a convergence of the calculation. This boundary setting will cause a fixed length for the center region, which differs from the boundaries during the tests. During the unloading and reloading process, the extended strip needed to be compressed at first, and then extended again toward the opposite direction. This compression effect led to the more severe hardened strength and a following pinching effect during the unloading and reloading process.

As indicated in Fig. 8, when the specimens achieved a large bending deformation, the applied load produced a longitudinal component force P (axial) along the length direction. This component force P (axial) caused a tensile bearing mode in the specimens. The proportion of the tensile resistance increased in cases with a larger rotation. Therefore, the steel strips presented the maximum strength increase in large amplitude cycles, particularly for specimens SS9 and SS10 (where a short transition length caused a larger bending rotation). The FE simulations also predicted this increase in strength, and even magnified the strength hardening effect under the boundary settings in the FE models. However, the FE models still achieved good predictions in accordance with the test data. The high stress locations and failure modes were also consistent with the test, indicating that the FE models can be applied for further investigation.

4.3. Discussion on connecting ring design

Specimens SS7 and SS8 exhibited an excessive plastic deformation at the connecting ring, which was consistent with the fracture failure mode in Fig. 6(e). Owing to the dramatic nonlinear deformation and high level of plasticity concentration in specimens SS7 and SS8, the lateral strength prediction from the finite element models presented relatively large deviations from the test data. In addition, the difference

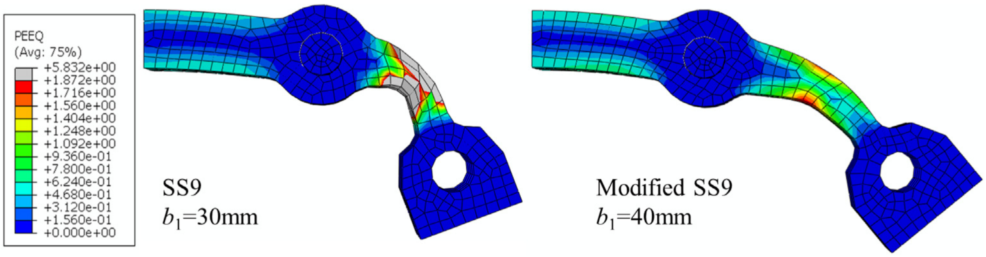

(a) PEEQ index distribution for specimen SS9 and the modified SS9 (Δ = 20 mm)

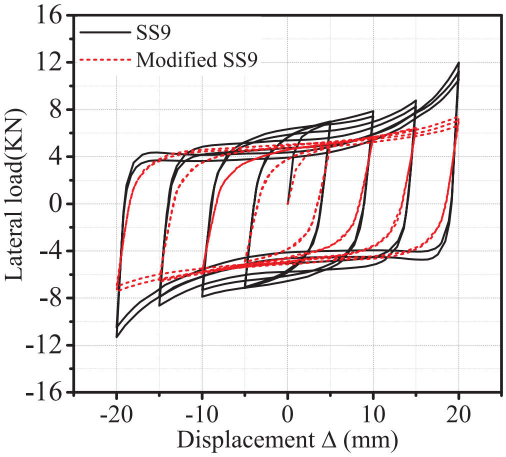

(b) Comparison of hysteretic relation

Fig. 17. Performance comparison of specimen SS9 and the modified SS9.

in strength was more prominent in specimen SS8 (Fig. 13), of which the nonlinear deformation at the connecting ring was more severe. The reason for this unfavorable failure mode was the weak design at the connecting ring, and a high level of plastic strain was developed and concentrated at the ring rib. Under the excessive plasticity development and the repeated tension-compression force and high extrusion force at the ring ribs (as illustrated in Fig. 8), ductile cracks were initiated and quickly expanded across the entire rib.

In the previous design, the width of the intermediate connecting ring was only 4.8 mm (the radius of the inner and outer arcs was 4.2 and 9.0 mm, respectively). By contrast, the minimum width calculated through Eq. (5) to ensure the shear safety was 4.9 mm for SS7 and 6.5 mm for SS8. To verify the effectiveness of Eq. (5), additional simulations were conducted on modified specimens SS7 and SS8, that the ring width of SS7 and SS8 was enlarged based on the minimum values calculated using Eq. (5). Fig. 15 shows comparisons of the stress state and hysteretic loop, and Fig. 16 provides a comparison of the PEEQ (equivalent plastic strain) index between the original specimens SS7 and SS8 and the modified SS7-SS8. The original SS7 and SS8 specimens presented a high PEEQ (Fig. 16) distribution at the ring rib, indicating an excessive plastic strain, whereas the modified specimens SS7 and SS8 presented a plasticity development mainly in the central and transition regions. The majority of the intermediate connecting ring still remained within the elastic state. Fig. 15(b) shows that a strengthened connecting ring construction will not present much effect on the yield strength. However, during large displacement loading cycles, the modification will change the failure modes from a connecting ring failure to the excessive bending failure at transition region. The latter strength degradations in original SS7 and SS8 were also changed to the additional strength increase mode owing to the tensile resistance under a large bending rotation.

The comparison proved that an enlarged ring width can ensure sufficient resistance at the connecting part. Therefore, a minimum width of the connecting ring needs to be determined in the steel strip design. This minimum width of the connecting ring can be calculated using Eq. (5). And the finally adopted ring width should be larger than this value, particularly under conditions with a short transition region.

4.4. Discussion on transition region design

The finite element results of specimen SS9 shown in Fig. 14 displayed a dramatic bending deformation and relatively higher level of plasticity development in the transition region. This result is consistent with the failure mode of specimen SS9 during the test (Fig. 6(f)), in which a dramatic bending and fracture failure occurred in the transition region. A previous discussion on the test data indicated that the reason for this failure mode might be the relatively weak design and the resulting large shear-bending force in the transition region. However, the deformation condition of the modified specimen SS8 in Fig. 13 indicates that a bending failure and tension loading mode in the transition region also took place in the wide strip case (h_0 = 8 mm, h_1 = 15 mm). To investigate the effect of the length of b_1 on the failure mode further, an additional model was established with the length of the transition region extended to 40 mm (the modified specimen SS9 in Fig. 14, with all other dimensions of the configuration remaining the same).

Fig. 17 shows the PEEQ index conditions and the hysteretic strength comparisons between the original and modified SS9 specimens. With a longer b_1, the relative bending rotation in the transition region was reduced under the same lateral displacement, thus reducing the requirement of the bending deformation and the plasticity development in the transition region. Fig. 17(b) indicates that the yield strength was reduced in the modified SS9 specimen, and the latter strength increase from the tension bearing under excessive bending rotation was significantly decreased. However, Fig. 17(a) shows a slightly higher level of plasticity development in the central region than that of the original SS9 specimen, representing more energy dissipation of the central

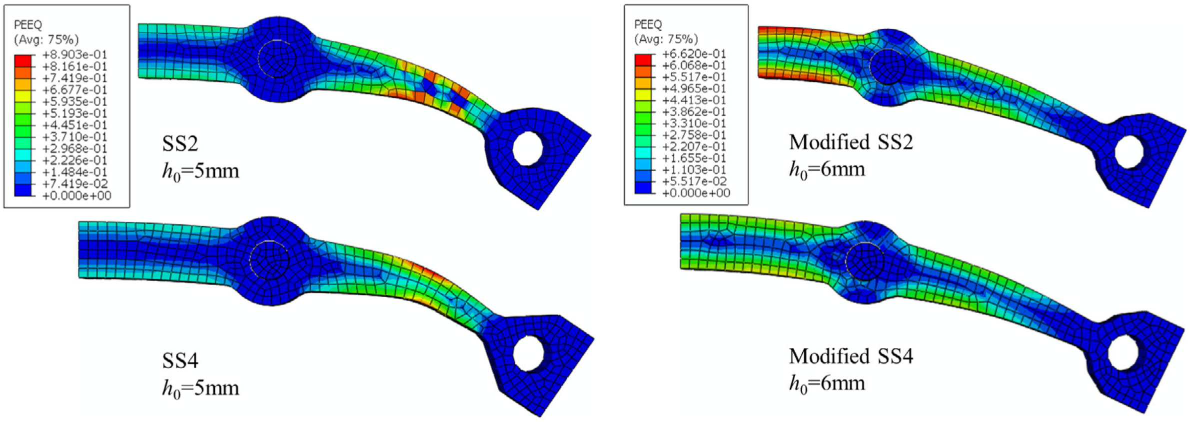

(a) Original design case

(b) Modified design case

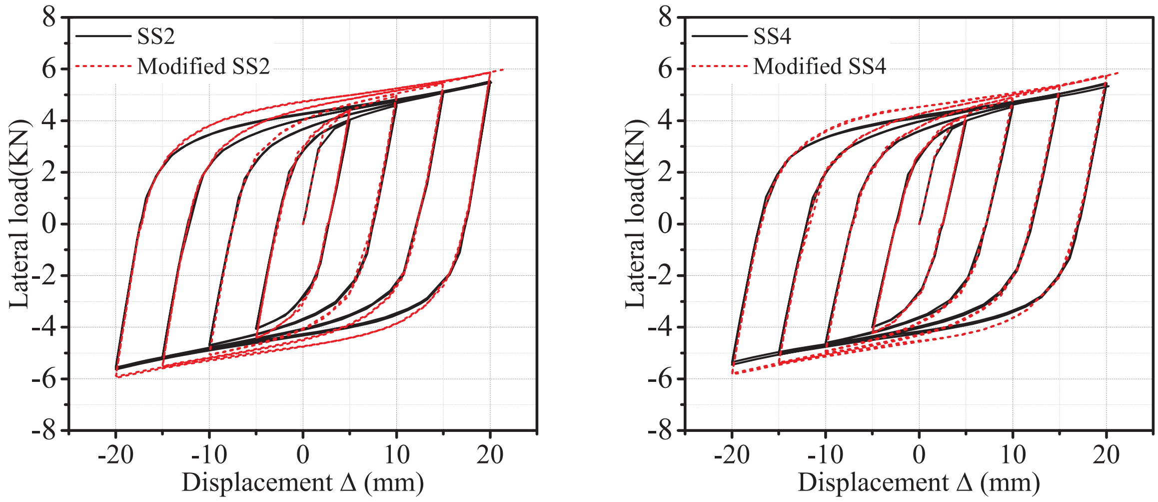

(c) Hysteretic relation comparisons

Fig. 18. PEEQ index distributions ($\Delta = 20$ mm).

region in the modified SS9 specimen. A similar improvement effect of a longer length of b_1 can also be reflected from the comparison between the modified SS7 and SS8 specimens shown in Fig. 16. Under the same lateral displacement, a longer length of b_1 represented a lower rotational demand in the transition region and a longer region for plasticity strain development. The plastic strain level can then be reduced, and the plasticity concentration and bending failure can be postponed and eliminated. Based on the test data and finite element results, the length of b_1 was suggested to be larger than 3 h_1 in a future design.

Specimens SS1, SS2, and SS4 had a 5 mm h_0, and the plastic stress development in the central region was relatively lower than that in the transition region (Fig. 14). However, for specimen SS5, the configuration had a dimensional relation of $h_0 = h_1/2$, and the extent of the plasticity was more uniform throughout the entire steel strip. Hence, two supplementary simulations were conducted with an increase in the h_0 length of the SS2 and SS4 specimens from 5 to 6 mm (half of h_1). Fig. 18 compares the PEEQ index conditions and the hysteretic results. The increase in h_0 did not present much variation in strength (Fig. 18(c)), although the plastic strain distribution was improved. In a previous design, the transition region had a higher level of plasticity development than the central region. However, with a 1 mm increase in h_0, the equivalent plastic strain distribution was dramatically improved: The PEEQ index distribution in the modified cases was more uniform throughout the entire strip and the peak PEEQ levels were reduced. The region with the main plasticity development changed from the transition region to the central region. Based on the present test data and finite element simulation results, h_0 was suggested to be no less than $h_1/2$ in the future design of a steel strip.

5. Summary and conclusions

In this study, a new metallic damper design was proposed featuring steep replaceable strip fuses and an adjustable design. Guidance regarding the primary configuration of the design of the fuse strips was given based on a theoretical derivation. The seismic performance of the steel strips was investigated through quasi-static tests and finite element analyses. In addition, some further design suggestions were given based on the results obtained.

(1) The proposed damper used bolted steel strips as the energy dissipation fuses, which can be replaced after failure without affecting the connecting parts. The steel strip participated in the load bearing and energy dissipation through the in-plane bending mechanism. The uniform central region and the construction of two varied transition regions can realize the simultaneous development of plasticity and energy dissipation throughout the entire strip range.
(2) The tested steel strips all displayed satisfactory bending ability and plasticity development with full hysteretic loops. Owing to a similar lateral strength development and energy dissipation performance, the theoretical parabolic transition can be replaced with straight

edges for a convenient fabrication. The bending moment strength of the steel strip was mainly controlled by the width of the central region.

(3) The sectional width in the central region determines the moment strength of the strips. The length of transition region b_1 transforms the moment strength of individual strips into the strength of the composed damper and can be used to adjust the lateral reaction force. And the transition region design can influence the plasticity development mode in the strips.

(4) The preliminary section design of the steel strip was given through a theoretical derivation. Together with the test data and finite element simulations, some additional design suggestions for the steel strips were given. The lower bound for the width of the connecting ring was suggested. The length of the transition region was suggested to be larger than three times the width in the central region. The minimum width at the two end supports was suggested to be no less than $h_1/2$ in the future design of the steel strip. However, a more systematic parametric study needs to be conducted in the future to reach more detailed influencing relations and detailed design guidance for the proposed damper.

Ethical statement

The work described has not been submitted elsewhere for publication, in whole or in part, and all the authors listed have approved the manuscript that is enclosed.

CRediT authorship contribution statement

Wei Guo: Supervision, Project administration. **Chenzhi Ma:** Investigation. **Yujie Yu:** Writing - review & editing, Investigation. **Dan Bu:** Software, Validation. **Chen Zeng:** Software, Validation.

Declaration of Competing Interest

The authors declare that they have no known competing financial interests or personal relationships that could have appeared to influence the work reported in this paper.

Acknowledgements

This research was sponsored by the National Natural Science Foundation of China (Grant No. 51878674, 51708402), the Foundation for Key Youth Scholars in Hunan Province (Project No. 150220077) and the Project of Yuying Plan in Central South University (Project No. 502034002).

References

[1] Constantinou MC, Soong TT, Dargush GF. Passive energy dissipation systems for structural design and retrofit, Seismic performance of steel plate slit-friction hybrid dampers; 1998.
[2] Soong T, Spencer Jr. B. Supplemental energy dissipation: state-of-the-art and state-of-the-practice. Eng Struct 2002;24(3):243–59.
[3] Lee J, Kang H, Kim J. Seismic performance of steel plate slit-friction hybrid dampers. J Constr Steel Res 2017;136:128–39.
[4] Connor JJ, Wada A, Iwata M, Huang Y. Damage-controlled structures. I: Preliminary design methodology for seismically active regions. J Struct Eng 1997;123(4):423–31.
[5] Symans M, Charney F, Whittaker A, Constantinou M, Kircher C, Johnson M, et al. Energy dissipation systems for seismic applications: current practice and recent developments. J Struct Eng 2008;134(1):3–21.
[6] Kelly JM, Skinner R, Heine A. Mechanisms of energy absorption in special devices for use in earthquake resistant structures. Bull NZ Soc Earthquake Eng 1972;5(3):63–88.
[7] Tapia N, Almazán J, Baquero J. Development of a novel combined system of deformation amplification and added stiffness and damping: analytical result and full scale pseudo-dynamic tests. Eng Struct 2016;119:61–80.
[8] Shih M-H, Sung W-P. A model for hysteretic behavior of rhombic low yield strength steel added damping and stiffness. Comput Struct 2005;83(12–13):895–908.
[9] Xu L-Y, Nie X, Fan J-S. Cyclic behaviour of low-yield-point steel shear panel dampers. Eng Struct 2016;126:391–404.
[10] Tsai K-C, Chen H-W, Hong C-P, Su Y-F. Design of steel triangular plate energy absorbers for seismic-resistant construction. Earthquake Spectra 1993;9(3):505–28.
[11] Mohammadi RK, Nasri A, Ghaffary A. TADAS dampers in very large deformations. Int J Steel Struct 2017;17(2):515–24.
[12] Garivani S, Aghakouchak A, Shahbeyk S. Numerical and experimental study of comb-teeth metallic yielding dampers. Int J Steel Struct 2016;16(1):177–96.
[13] Black CJ, Makris N, Aiken ID. Component testing, seismic evaluation and characterization of buckling-restrained braces. J Struct Eng 2004;130(6):880–94.
[14] Xie Q. State of the art of buckling-restrained braces in Asia. J Constr Steel Res 2005;61(6):727–48.
[15] Mahrenholtz C, Lin PC, Wu AC, Tsai KC, Hwang SJ, Lin RY, et al. Retrofit of reinforced concrete frames with buckling-restrained braces. Earthquake Eng Struct Dyn 2015;44(1):59–78.
[16] Chan RW, Albermani F. Experimental study of steel slit damper for passive energy dissipation. Eng Struct 2008;30(4):1058–66.
[17] Jacobsen A, Hitaka T, Nakashima M. Online test of building frame with slit-wall dampers capable of condition assessment. J Constr Steel Res 2010;66(11):1320–9.
[18] Kurata M, He L, Nakashima M. Steel slit shear walls with double-tapered links capable of condition assessment. Earthquake Eng Struct Dyn 2015;44(8):1271–87.
[19] Hedayat AA. Prediction of the force displacement capacity boundary of an unbuckled steel slit damper. J Constr Steel Res 2015;114:30–50.
[20] Ghabraie K, Chan R, Huang X, Xie YM. Shape optimization of metallic yielding devices for passive mitigation of seismic energy. Eng Struct 2010;32(8):2258–67.
[21] Lee C-H, Ju YK, Min J-K, Lho S-H, Kim S-D. Non-uniform steel strip dampers subjected to cyclic loadings. Eng Struct 2015;99:192–204.
[22] Kim J, Choi H. Behavior and design of structures with buckling-restrained braces. Eng Struct 2004;26(6):693–706.
[23] Aghlara R, Tahir MM. A passive metallic damper with replaceable steel bar components for earthquake protection of structures. Eng Struct 2018;159:185–97.
[24] Lee J, Kim J. Development of box-shaped steel slit dampers for seismic retrofit of building structures. Eng Struct 2017;150:934–46.
[25] Shi Y, Wang M, Wang Y. Experimental and constitutive model study of structural steel under cyclic loading. J Constr Steel Res 2011;67(8):1185–97.